Research Article

Crack Propagation and Fragmentation Characteristics of Single-Flawed Sandstone Samples under Different Loading Conditions

Wen Lei,[1] Feng Wenjie,[2] Li Mingye [ID],[3] and Yu Junhong[4]

[1]*Department of Engineering Mechanics, Hebei Key Laboratory of Mechanics of Intelligent Materials and Structures, Shijiazhuang Tiedao University, Shijiazhang 050043, China*
[2]*Shijiazhuang Tiedao University, Shijiazhang 050043, China*
[3]*Hebei Polytechnic Institute, Shijiazhang 050091, China*
[4]*Department of Engineering Mechanics, Shijiazhuang Tiedao University, Shijiazhang 050043, China*

Correspondence should be addressed to Li Mingye; 363811687@qq.com

Red sandstone specimens with preexisting single flaw were taken as the research object in the static and dynamic loading tests. A hydraulic press was used for the uniaxial compression experiment, and SHPB was used for the impact test. The corresponding static and dynamic stress-strain curves were obtained. The crack propagation of rock samples under different loading conditions was obtained using the camera system. The crack propagation, compressive strength, and energy characteristics of samples under quasi-static and dynamic impact loading were analyzed. The findings show that the crack initiation, development, and final fracture mode of the samples are closely related to the inclination angle of preexisting flaw and strain rate. Compared with samples under static loading, tensile and shear mixed cracks, layer separation cracks, and more far-field cracks appeared in the samples under dynamic loading. With the increase of the peak of incident wave during the SHPB test, the samples with preexisting flaw change from tensile crack to X-shaped shear failure in the range of medium strain rate. Under different loading conditions, the compressive strength of samples with 45° crack is the lowest. The energy dissipation density and energy dissipating rate of the single-flawed specimens feature a rising trend with the increasing peak of incident wave, and the influence of the inclination angle of preexisting flaw on the energy dissipation is significant for a given peak of incident wave. The strength, energy dissipation, and fractal dimension of the specimens are positively correlated with each other under different strength impact loading. As the peak of incident wave increases, the inclination angle of preexisting flaw has more significant influence on the interrelation of these three parameters.

1. Introduction

The macroscopic cracks are staggered and dispersed in engineering rock mass. The fractured rock mass may be unstable and fail under static and dynamic loads such as geostress field, earthquakes, blasts, and mechanical vibration. The failure of rock is often related to existing cracks. Under different loading conditions, the failure modes of the rock mass are usually different. Therefore, it is of great practical significance for the safety of rock engineering to study the influences of precrack on rock fracturing behavior and energy dissipation.

In the past few decades, the mechanical properties and crack propagation of rocks with precracks have been studied

by many scholars. It is very difficult to study the fracturing behavior of rocks using theoretical analysis methods because rock is usually heterogeneous [1, 2]. Therefore, experiments are thought to be the main method for studying the fracturing behavior of rocks containing precracks under static or dynamic loading. Under static loading, the discussion on the fracture of fractured rocks started earlier and was studied more thoroughly. For instance, Yang et al. [3] studied the effect of precrack shape on the compressive strength and fracture behavior of rocks under quasi-static compression condition. Bobet et al. [4] made rock-like samples with double precracks, analyzed the law of fracture dislocation, initiation, and propagation of new cracks, and discussed the

relationship between the distribution of cracks and the final failure mode under static compression loading. Huang et al. [5] and Haeri et al. [6], respectively, summarized 5 crack growth modes and 9 crack types of flawed rock under static loading conditions through experiments. Zhou et al. [7] discussed 5 types of cracks in rock samples, and 10 types of crack coalescence forms are summarized based on the analysis of crack evolution process. Shen-Qi and Hong-Wen [8] analyzed the influence of single precrack on the compressive strength and deformation behavior of rock samples based on the experimental results of static stress-strain curves, and nine crack types were summarized. Zhao et al. [9] took rock-like specimens containing two precracks as the research objects and conducted a number of static compression tests. Four different types of cracks were observed in the experiments.

Strength characteristics and the fracture behavior of intact rock under impact load have been well understood in previous studies. It is long recognized that the rock strength is rate-dependent under dynamic loading [10, 11]. The fracture behavior of rock with precracks is different under dynamic load and static load [12]. The dynamic failure mode of intact rock is rate-dependent [13, 14]. Although the research on dynamic mechanical properties and dynamic crack propagation of rock with precracks started later comparatively, many results have been obtained. For instance, Li et al. [15] took slab marble as the research object and studied the effect of precrack angle on the dynamic mechanical properties using a modified split-Hopkinson pressure bar (SHPB) device at strain rates of 37.8–83.9 s^{-1}. Six crack growth types were summarized and compared with the crack growth modes under static loading by other scholars. Zou et al. [16] obtained seven crack types of rectangular plate samples with one preexisting crack and summarized the fracture modes under various strain rates of 120–170 s^{-1}. Li et al. [12] took the square slab marble with one or two preexisting cracks as the research object, analyzed the rock mass fracture mode under dynamic impact loading, and summarized 9 failure types of the samples with two preexisting cracks. Dong et al. [17] recorded and studied the crack propagation process of rock-like plates with one precrack using SHPB and ultra-high-speed camera system. Recently, Han et al. [18] did a lot of experiments for investigating the effects of precrack angle and initial static load on the crack propagation process of rock specimens under dynamic loading. You et al. [19] studied the influence of precrack on the dynamic mechanical properties and failure modes of sandstone under different confining pressures and different strain rates. The numerical simulation study shows that the failure mode of rectangular specimens with single flaw under the impact loading condition is related to the loading rate [20].

Under the condition of medium strain rate, the influences of preexisting flaw parameters (i.e., size and inclination angle) on dynamic mechanical properties and crack propagation have been discussed, and the influences of strain rate on crack progressive growth behavior have also been studied. However, relevant experimental results within the range of medium strain rate are not sufficient. Specially,

the gas pressure for driving the striker of the SHPB device is often kept constant during SHPB tests in the past study, resulting in neglect of strain rate effect of failure modes of flawed rock samples. In view of this, studying the related problems under dynamic loading in the range of medium strain rate is essential for rocks with precracks. It is known that mechanical properties of samples are closely related to their size, and relevant studies also show that the crack propagation of rock is closely related to its size too [12]. Square or cylindrical specimens are used in SHPB experiments for discussing the problem of crack propagation frequently. Some scholars generally apply dynamic impact load in the direction of sample length in order to compare with the static experimental results when the rectangular plate specimen is used in SHPB experiment. However, according to the principle of SHPB experiment, it is important to have sufficient number of stress waves propagating back and forth in the sample. If rock samples with a length-to-width ratio greater than 1 : 1 are subjected to impact dynamic load along the length direction, it is not easy for long rock samples to meet the stress equilibrium condition in the SHPB test. The International Society for Rock Mechanics (ISRM) recommends height-diameter ratios between 0.5 : 1 and 1 : 1 for rock samples in SHPB tests, so the impact dynamic load is applied along the width direction of the sample in this study; at the same time, the inertial effect can be better weakened.

In this study, the static and dynamic load tests were carried out using the same finite size rock samples with one precrack. The corresponding static and dynamic loads were applied along the length or width of the samples. The angle between static load direction and precrack is the same as that between dynamic load direction and precrack by setting the inclination angle of the flaw with a reciprocal relationship. The inclination angle of the precrack includes 0° and 90°, 30° and 60°, and 45° in this study. The static mechanical properties and fracture mode under the influence of precrack were studied using the hydraulic servo loading system with a camera. The dynamic mechanical properties and crack evolution under the influence of precrack and strain rate were investigated using the SHPB equipment with a high-speed camera system. The results of mechanical properties, fracture behavior, and energy dissipation under these different loading conditions are compared and analyzed.

2. Experimental Setup

2.1. Specimen Preparation. The experiments took red sandstone as the research object in this paper. Red sandstone used in these experiments is made of quartz, feldspar, calcite, and illite. The red sandstone samples used in these tests were taken from the same rock block of an underground mine in Hunan Province of China, which is a common type of mine surrounding rock in this area.

Under axial load, crack mode on the surface of cylindrical specimen is different from that inside the sample [20, 21], so the rock samples were processed into thin plate shape rather than a cylinder in this study. Following the

method recommended by ISRM [22] and considering the diameter of the bar of the SHPB device, the ratio of length to width of the samples is set about 0.65 with a nominal size of $46 \times 30 \times 15 \, mm^3$ but with different flaws. The two ends of the sample were smoothed to a nonuniformity less than ±0.05 mm, and the nonperpendicularity of the adjacent two sides was within ±0.25°.

Before the flaw of sample was prefabricated, P-wave velocity of the samples was measured using wave velocity measuring instrument, dry density was measured by a high-precision electronic balance, electric blast drying oven, and caliper, and saturated water absorption rate was measured by high-precision electronic balance and vacuum water saturation instrument. The dry density of the samples is 2.37 g/ cm^3–2.39 g/cm^3 (the average is 2.38 g/cm^3), the saturated water absorption rate is 3.11%–3.25% (the average is 3.18%), and dry p-wave velocity is 2286 m/s–2324 m/s (the average is 2299 m/s).

An 8 mm penetrating fissure is prefabricated in the center of the sample using the central drilling method. The angles between the precrack and length direction of the sample are, respectively, 0°, 30°, 45°, 60°, and 90°. These angles are complementary to each other. The pictures of the parts of samples are shown in Figure 1.

For reducing the end effect in tests, the samples were loaded along the length direction in the static load test, while the samples were loaded along the width direction in the dynamic impact test. This ensures that the geometry of the specimens and prefabricated flaws is identical in static and dynamic tests. In the static load tests, the samples were divided into 5 groups according to the inclination angles of prefabricated flaws, and 3 samples constituted a group. A total of 15 specimens were tested under static uniaxial compression. In the SHPB test, the samples are divided into 20 groups according to the peak of incident wave and the inclination angles of prefabricated flaws. A total of 60 specimens were tested under impact loading.

2.2. Testing Installation.

Static load tests were carried out according to the suggestions proposed by the professional standards compilation group of people's republic of China (SL264-2001). The quasi-static compression test is performed on a hydraulic servo loading system. A camera with a resolution of 4096×3000 and a refresh rate of 30 Hz was used to record crack propagation path. The change of strain rates has little effect on the strength of rock under the condition of quasi-static strain rate [16]. In the compression test, the loading rate is fixed at 0.5 MPa/s until the specimens were damaged. In order to reduce the transverse frictional resistance between the specimen and the equipment, some lubricant was spread on the surfaces of the specimen. The device of static loading experiment and the relationship between the specimen placement direction and loading direction are shown in Figure 2, where P_s denotes static load and β denotes the angle between the precrack and loading direction.

The SHPB was used for dynamic load tests, which is made of 40 Cr alloy steel. The SHPB device consists of an air gun, an incident bar (3 m in length), a transmitted bar (2 m),
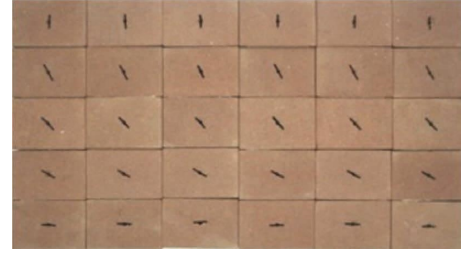

FIGURE 1: A part of samples.

an absorbing bar (1 m), and a set of data acquisition and analysis system. The diameter, P-wave velocity, density, and elastic modulus of the bars of SHPB equipment are 5 cm, 5410 m/s, 7810 kg/m^3, and 210 GPa, respectively. The cone-shaped striker was used for producing a half-sine wave aimed to eliminate wave dispersion [23]. Crack propagation path was recorded by an ultra-high-speed camera during impact loading. Considering the resolution and image brightness, the acquisition frequency of the camera was set to 75,000 fps. The SHPB device is shown in Figure 3, where P_d denotes dynamic load. The specimen number represents loading mode (P_s or P_d), flaw inclination angle (β), and sample serial number. "S" indicates static loading and "D" indicates dynamic loading in the sample number. For example, D-30-3 denotes the third single-flawed sample with $\beta = 30°$ under dynamic load.

The peak of incident wave (strain rate of specimens) depends on the speed of the cone-shaped bullet. The striker velocities in SHPB tests were set as 6 m/s, 8 m/s, and 10 m/s by adjusting the pressure of the air gun. Under different striker velocities, the peaks of incident waves were 40.7 MPa, 61.1 MPa, and 76.5 MPa, respectively. The strain rates of the samples were $37.8 \, s^{-1} \sim 45.8 \, s^{-1}$, $55.3 \, s^{-1}$ $65.8 \, s^{-1}$, and $75.3 \, s^{-1} \sim 83.9 \, s^{-1}$, respectively. Due to the diverse dip angle of precracks, the propagation of stress waves in the samples is different. The generated transmitted and reflected waves are different because of the precrack, so the strain rate of the samples with diverse precracks changes under the same incident wave condition.

3. Experimental Results

3.1. Static Mechanical Properties.

The static stress-strain curves (σ-ε curves) of the samples under static compression are shown in Figure 4. The specimens generally show the characteristics of brittle fracture in the tests, and there was loud sound when the specimens broke. The static σ-ε curve can be roughly divided into 4 parts. In the first stage (compaction stage), the σ-ε curve presents a microcurved shape, and the micropores in the specimen are gradually closed. However, it can be seen from the photographic images that there is no obvious compression collapse phenomenon in the precrack of the sample. In the second stage (elastic deformation), the σ-ε curve is approximately straight, and linear elastic deformation occurs along the load direction. In the third stage (crack propagation), the new crack starts and develops around the preexisting flaw, leading to nonlinear deformation of the rock. In the last
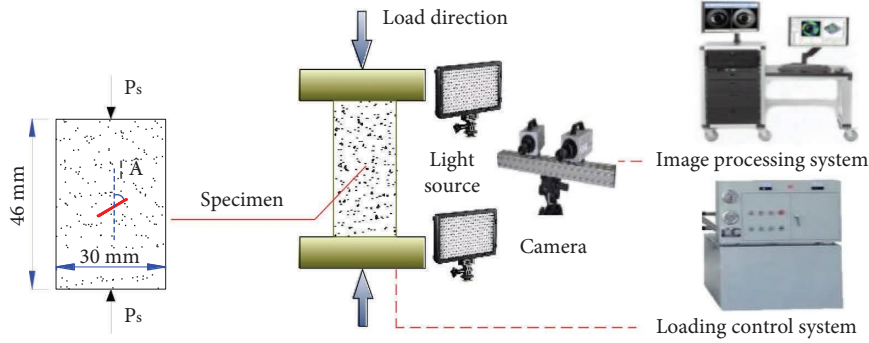
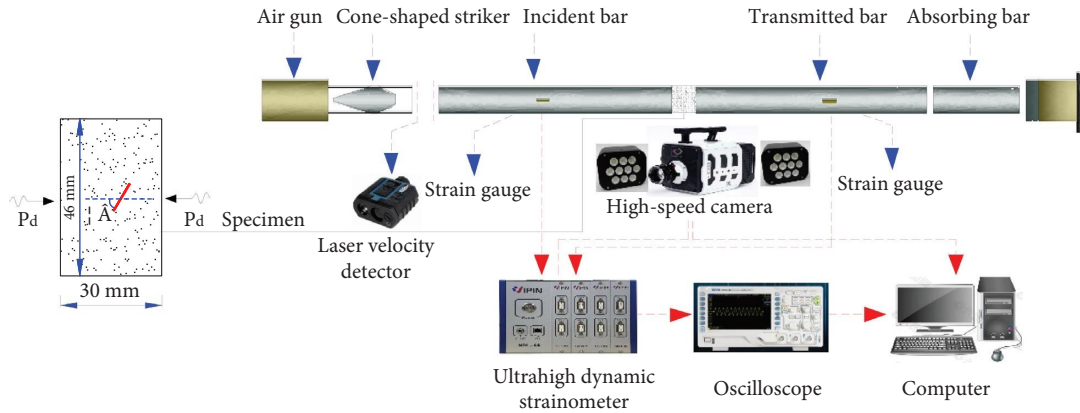FIGURE 2: Device of static uniaxial compression test.
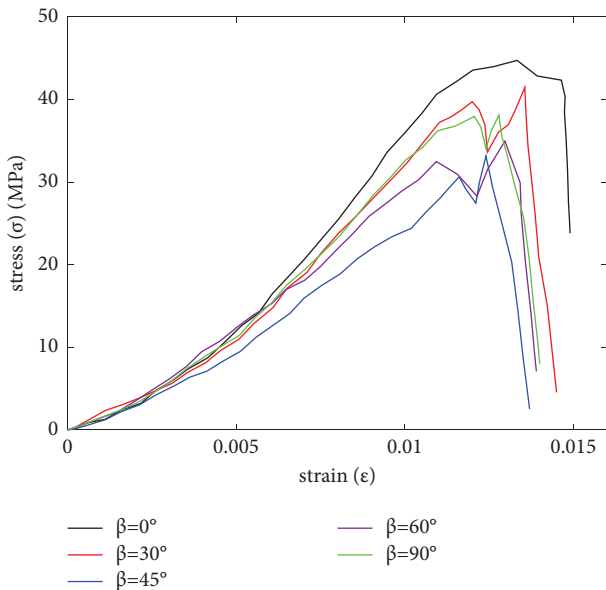

FIGURE 3: SHPB test equipment.

FIGURE 4: Static stress-strain curves.

stage (failure stage), some through cracks are formed, and the rock strength drops rapidly. Under static loading, stress concentration is generated around the precrack, resulting in new crack initiation and propagation in stages. Stress-strain curves have double peak because of internal crack of rock

extension, penetration, and friction under the effect of sustained loading. Static uniaxial compressive strength (UCS) and elastic modulus (E_0) of specimens with different precrack are listed in Table 1.

With the increase of β angle, the UCS decreases first and then increases. The strength of 45° sample is minimum, and the strength of 0° sample is maximum. The values of strength of all the samples for static uniaxial compressive test are between 33.15 MPa and 44.73 MPa. The static elastic modulus ranges from 3.22 GPa (45° sample) to 4.65 GPa (0° sample), which has a similar tendency with the UCS.

3.2. Dynamic Mechanical Properties

3.2.1. Stress Balance. The dynamic stress balance is the premise for effective results of SHPB experiment, especially for samples containing penetrating fissure [24]. In this study, a cone-shaped bullet was used for producing a half-sine wave aimed to help with stress equilibrium at the two ends of the specimen and help with providing constant strain rate loading [15].

The incident wave, reflected wave, and transmitted wave were picked up by the strain gauges on the bars of SHPB equipment. The typical waves obtained by SHPB test in this study are shown in Figure 5 (signal-i, signal-r, signal-t, and signal-$i + r$ represent incident wave, reflected wave, transmitted wave, and superposition of the incident wave and reflected wave, respectively). The superposition of the

TABLE 1: Mechanical parameters of specimens under static uniaxial compression.

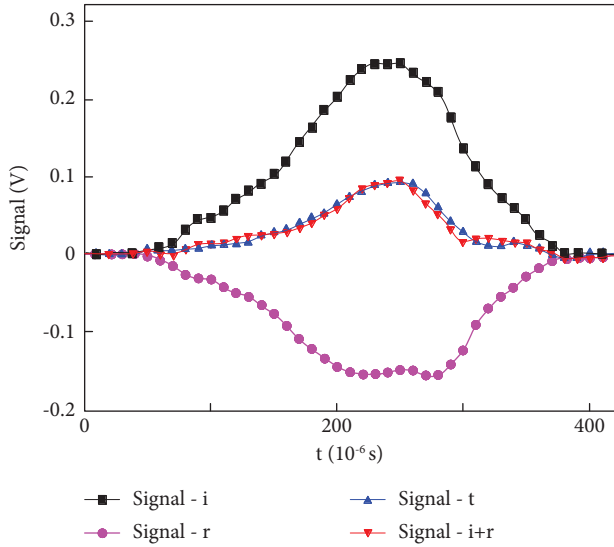| β (°)	UCS σ_c (MPa)	E_0 (GPa)
0	44.63	4.76
30	40.45	4.39
45	33.15	3.22
60	34.96	3.55
90	38.09	3.94

FIGURE 5: Typical incident, reflected, and transmitted waves.

incident wave and reflected wave basically overlaps with the transmitted wave, which indicates that the sample meets the stress balance condition. All the SHPB test results of this study were verified by stress equilibrium before the test data analysis.

"3-wave analysis" method [25] containing incident wave $\varepsilon_I(t)$, reflected wave $\varepsilon_R(t)$, and transmitted wave $\varepsilon_T(t)$ can be used to calculate the strain ($\sigma(t)$), stress ($\varepsilon(t)$), and strain rate ($\dot{\varepsilon}(t)$). The formulas of the "3-wave analysis" method are expressed as

$$\sigma(t) = \frac{E_e A_e}{2A_s}\left[\varepsilon_I(t) - \varepsilon_R(t) + \varepsilon_T(t)\right],$$

$$\varepsilon(t) = \frac{C_e}{L_s}\int_0^t \left[\varepsilon_I(t) + \varepsilon_R(t) - \varepsilon_T(t)\right]dt, \quad (1)$$

$$\dot{\varepsilon}(t) = \frac{C_e}{L_s}\left[\varepsilon_I(t) + \varepsilon_R(t) - \varepsilon_T(t)\right],$$

where A_s and A_e denote the cross-sectional area of the sample and the steel bars of SHPB equipment, respectively, L_s denotes the length of the specimen, and E_e and C_e denote Young's modulus and longitudinal wave velocity of the steel bars, respectively.

3.2.2. Dynamic Stress-Strain Curves. Taking the specimens with strain rate around $60\,s^{-1}$ as examples, the dynamic σ-ε curves of specimens with different precrack angles are shown

in Figure 6. Taking samples with precrack angle $\beta = 60°$ as examples, the σ-ε curves of samples with different strain rates are shown in Figure 7.

The dynamic σ-ε curves have no compaction stages compared to static stress-strain curves. Clearly, the preexisting flaw and strain rate have important impact on the σ-ε curves of the rock samples. With the increase of strain rate, the peak stress and the dynamic modulus of elasticity increase significantly when the flaw angle is constant. Meanwhile, the peak stress and the dynamic modulus of elasticity change, depending on the increase of flaw angle when the peak of incident wave is constant. However, the precrack angle has no obvious impact on the peak strain of σ-ε curves.

3.2.3. Dynamic Strength and Modulus of Samples. The mechanical parameters of the tested samples with different β values and strain rates are listed in Table 2. The parameters $\dot{\varepsilon}$, σ_d, and E_d are denoted as strain rate, dynamic compressive strength, and dynamic modulus of elasticity of samples in Table 2, respectively.

The dynamic strength and the modulus of elasticity of the samples with different strain rates are plotted against the β values in Figure 8. With the increase of precrack angle, strength (σ_d) decreases first and then increases, which is similar to the static strength. The dynamic strength of samples with $\beta = 45°$ is the minimum, which is similar to the static experiment results. The dynamic strength of samples with $\beta = 60°$ or $\beta = 0°$ is the maximum with the change of peak of incident wave. Under static loading, the static strength of 0° sample is the highest, which is 134.6% of that of 45° sample. When the peak of incident wave is about 40.7 MPa, the strength of the rock specimens with $\beta = 60°$ is the highest, which is 123.5% of that of the 45° sample. When the peak of incident wave is 61.1 MPa, the dynamic strength of 0° sample is the highest, which is 123.7% of that of 45° sample. When the peak of incident wave is 76.5 MPa, the strength of the rock specimens with $\beta = 0°$ is the highest, which is 122.6% of that of the 45° sample. The ratio of minimum and maximum of strength of rock samples with different β values is very similar, which is less than that of static strength slightly. With the increase of peak of incident wave, the dynamic modulus of elasticity increases, which is consistent with strain rate impact of dynamic compression strength.

Under impact load, the growth factor of dynamic strength (DIF) is the ratio of dynamic strength and static strength, which can be used as an indicator of strength growth [26]. The DIF values of the samples are listed in Table 3. Equation (2) is suitable to reflect the strain rate impact of rock strength in the range of medium strain rate [26].

$$\text{DIF} = a \cdot e^{b\dot{\varepsilon}}, \quad (2)$$

where a and b are fitting parameters. The parameter b reflects the strain rate correlation of samples. The fitting curves of DIF values against the strain rate of samples with different β values are plotted in Figure 9. The relevant parameters of equation (2) are listed in Table 4.
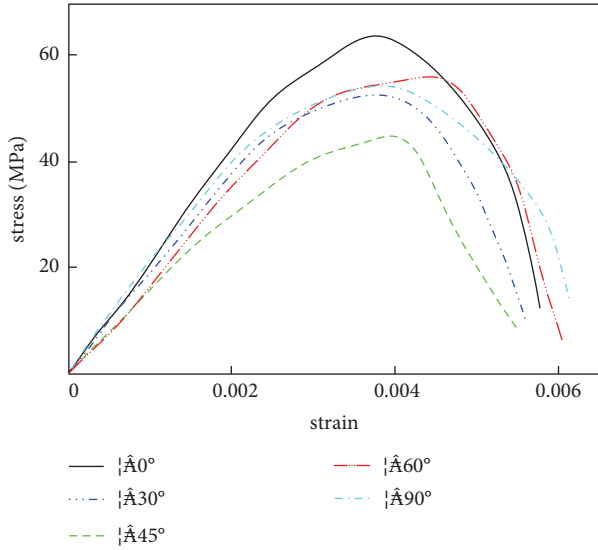
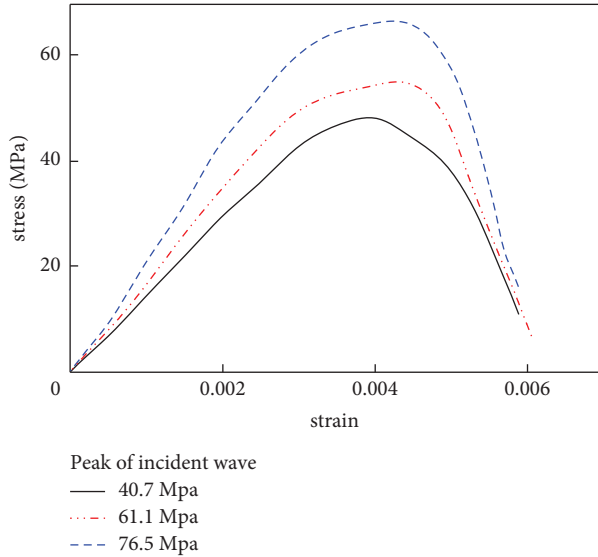Figure 6: Stress-strain curves of samples with different dip angles.

Figure 7: Stress-strain curves of different strain rates.

Table 2: Dynamic mechanical parameters of samples.

Specimen number	$\dot{\varepsilon}$ (s^{-1})	σ_d (MPa)	E_d (GPa)
D-0-4	41.3	48.7	10.28
D-0-5	38.7	45.2	9.67
D-0-6	40.9	44.8	10.67
D-0-7	65.8	64.9	16.78
D-0-8	60.4	61.9	15.24
D-0-9	57.2	57.3	15.97
D-0-10	76.8	79.8	20.81
D-0-11	82.3	81.1	21.02
D-0-12	83.2	83.5	20.44
D-30-4	37.8	40.8	8.78
D-30-5	42.3	43.5	9.34
D-30-6	39.8	41.7	9.03
D-30-7	55.6	55.2	14.58
D-30-8	59.7	58.8	15.20
D-30-9	62.1	54.3	13.91
D-30-10	76.5	76.2	16.45
D-30-11	79.8	79.3	17.28
D-30-12	83.2	78.5	16.92
D-45-4	40.8	39.7	7.01
D-45-5	39.7	41.2	7.58
D-45-6	43.2	42.8	6.98
D-45-7	55.3	45.3	10.94
D-45-8	59.7	50.8	11.98
D-45-9	62.5	52.8	12.04
D-45-10	80.2	60.1	14.58
D-45-11	83.7	65.8	15.21
D-45-12	78.9	63.2	14.07
D-60-4	38.8	48.8	7.54
D-60-5	43.5	50.2	8.01
D-60-6	41.3	53.8	7.81
D-60-7	59.7	55.7	13.27
D-60-8	63.2	59.8	13.29
D-60-9	58.6	55.7	13.74
D-60-10	75.3	62.7	18.79
D-60-11	79.4	66.8	17.01
D-60-12	83.2	67.8	18.61
D-90-4	39.7	50.1	8.94
D-90-5	45.8	53.2	9.51
D-90-6	42.1	47.8	8.74
D-90-7	62.1	52.1	14.31
D-90-8	60.7	54.9	14.97
D-90-9	65.2	59.8	15.21
D-90-10	77.9	69.4	19.41
D-90-11	83.9	72.8	20.21
D-90-12	79.8	70.1	19.78

It is evident that the sensitivity of dynamic strength to strain rate of samples with different flaws is different. In the range of 40 s^{-1}–80 s^{-1} strain rate, the b value of sample with flaw of $\beta = 30°$ is the largest relatively. It indicates that the dynamic strength of sample with $\beta = 30°$ increases the most with the increase of strain rate. In contrast, b value of rock specimen with $\beta = 60°$ is relatively minimum, indicating that for this rock specimen with $\beta = 60°$, the impact of strain rate on strength is the weakest.

4. Fracture Behaviors

4.1. Crack Types. The macroscopic crack is the result of the propagation of microcrack in rock sample and expansion of new cracks under the external loads and other factors. The complicated stress environment in the rock samples can cause tensile cracking or shear cracking.

Many studies in the past have been conducted on the crack propagation path of rocks by static or dynamic load tests. Many results of quasi-static tests showed that 3 molds of new crack could be observed during static loading: wing crack, antiwing crack, and secondary crack [8, 27]. Tensile crack includes the wing crack and antiwing crack; meanwhile, shear crack includes oblique secondary crack and coplanar secondary crack (Figure 10). More secondary cracks (shear cracks) have been observed during many dynamic load tests [16, 28]. Those kinds of shear cracks are the secondary cracks shown in Figure 10. The tensile cracks are initiated firstly during static load tests [8]. On the contrary, the tensile cracks initiated later than shear cracks
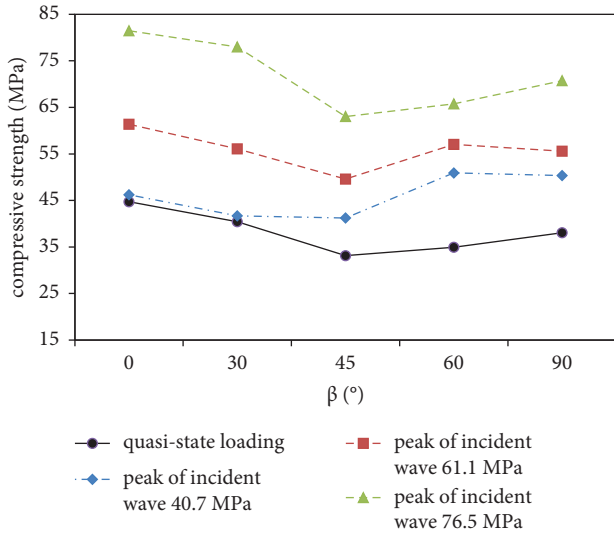
FIGURE 8: Relationship between dynamic compressive strength and crack angles.

TABLE 3: Growth factor of dynamic strength.

Specimen number	DIF
D-0-4	1.09
D-0-5	1.01
D-0-6	1.01
D-0-7	1.45
D-0-8	1.39
D-0-9	1.28
D-0-10	1.79
D-0-11	1.82
D-0-12	1.87
D-30-4	1.01
D-30-5	1.08
D-30-6	1.03
D-30-7	1.36
D-30-8	1.45
D-30-9	1.34
D-30-10	1.88
D-30-11	1.96
D-30-12	1.94
D-45-4	1.20
D-45-5	1.24
D-45-6	1.29
D-45-7	1.37
D-45-8	1.53
D-45-9	1.59
D-45-10	1.81
D-45-11	1.98
D-45-12	1.91
D-60-4	1.40
D-60-5	1.44
D-60-6	1.54
D-60-7	1.59
D-60-8	1.71
D-60-9	1.59
D-60-10	1.79
D-60-11	1.91
D-60-12	1.94
D-90-4	1.32
D-90-5	1.40
D-90-6	1.25
D-90-7	1.37
D-90-8	1.44
D-90-9	1.57
D-90-10	1.82
D-90-11	1.91
D-90-12	1.84

during dynamic load tests [15, 28]. Therefore, in this paper, crack types are divided into shear cracks and tensile cracks according to crack propagation mechanism, rather than naming "secondary crack." Tensile cracks are usually clean and straight in character and generally exhibit plumose textures. In contrast, shear cracks are usually rough, which are often filled with pulverized rock debris.

The crack types according to geometry of crack propagation path under dynamic impact loading are summarized by Li et al. [15] and Zou et al. [16], and those under static load are summarized by Wong et al. [29] and Yang et al. [3]. According to the crack types summarized by those relevant scholars and phenomenon observed in the present experiments, nine crack types with different initiation mechanisms (shear or tensile) and geometries were proposed in this paper (Figure 11). "T" and "S" in Figure 11 represent tensile and shear crack, respectively. The "separation layer crack" (type IX) is separated from the type of far-field crack (type VIII proposed by Li et al. [15] and Li et al. [12], which is caused by tensile stress formed by reflection of stress wave). Type VIII crack is characterized by propagating along the loading direction; in contrast, type IX crack propagates perpendicularly to the loading direction. According to the angle between direction of crack initiation and precrack, types I, II, and III are separated from the type of tensile crack proposed by Li et al. [15]. Types I, II, III, VIII, and IX are tensile cracks, types V, VI, and VII are shear cracks, and type IV is a mixed tensile-shear crack. Compared with Figure 10, type IV and three kinds of far-field cracks, VII, VIII, and IX, are proposed in this paper, which are more suitable for describing dynamic experimental results. Characteristics of each type of crack are described as follows.

Type I tensile cracks generate near the precrack tips or at the middle of the flaw, propagate perpendicularly to the flaw, and then transform to grow along the direction of external load. Type II tensile cracks generate along the precrack direction and then transform to grow along the direction of

external load. Type III tensile cracks generate near precrack tips and grow along the direction of load. Type IV mixed tensile-shear cracks first propagate near the precrack tips as shear cracks and then become tensile cracks and grow along the load direction. Compared with type II tensile cracks, type IV cracks usually are covered with pulverized rock debris near the tips of the precrack. Type V oblique shear cracks usually generate near the precrack tips, at an angle with the loading direction. The cracks are often characterized by shear bands filled with rubble powder. Type VI quasi-coplanar shear cracks usually generate near the precrack tips and grow along the precrack direction. Type VII far-field shear cracks and type VIII and type IX far-field tensile cracks
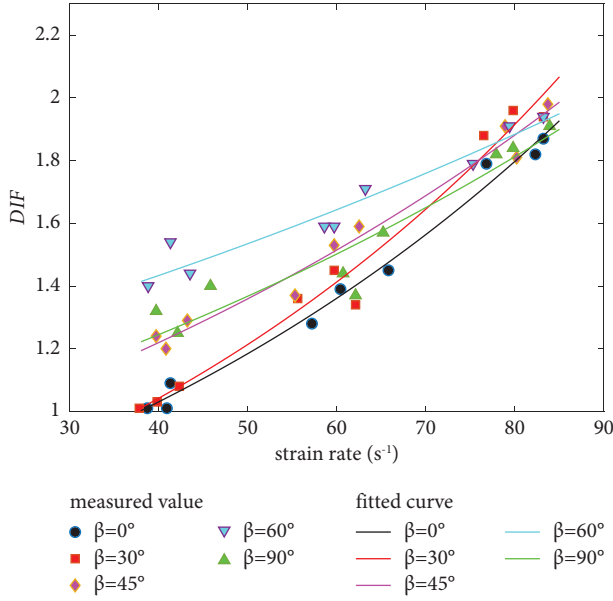
FIGURE 9: The fitting curves of DIF value.

TABLE 4: Related parameters.

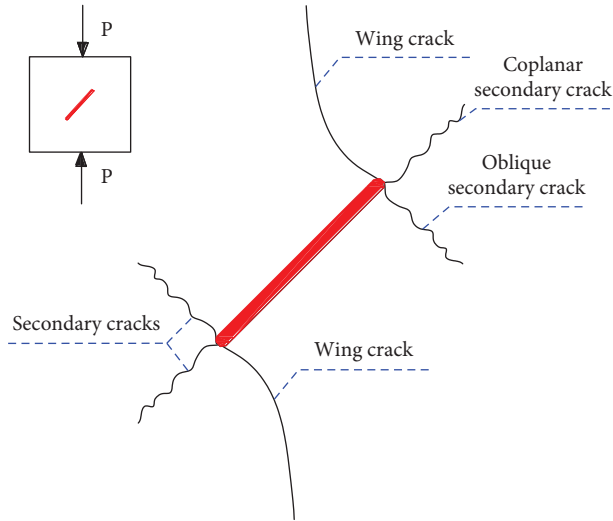| β	0°	30°	45°	60°	90°
a	0.5908	0.5670	0.7906	1.0910	0.8552
b	0.0139	0.0152	0.0108	0.0068	0.0094

FIGURE 10: Types of new cracks during static loading.

initiate far from the precrack, which generally initiate during the late stage of dynamic load except for a few samples. The directions of type VIII and type IX are perpendicular to each other.

4.2. Failure Modes

4.2.1. Fracture Mode under Static Loading. For single-flawed samples, different failure modes were observed under uniaxial compression. Ultimate broken patterns of the single-

flawed samples are distinctly dependent on the flaw geometry. The rock samples were generally broken into several main parts at failure. Crack types I, II, III, V, and VI were identified by studying the ultimate broken patterns of the single-flawed samples (Figure 12). Most of the ultimate broken patterns of the samples with precrack contain a variety of crack forms.

The crack propagation path of samples with different precracks is as follows.

Firstly, a new crack initiated and propagated vertically upward along the prefabricated crack in the sample with $\beta = 0°$, and then type V oblique shear cracks propagated toward the boundaries of the sample. The crack propagating vertically upward is sliding mode crack, which can be classified as type VI quasi-coplanar shear crack because the propagation path of this new crack is consistent with the theoretical solution of the initiation angle of the shear crack [28]. The two kinds of cracks in the sample with $\beta = 0°$ initiated continuously, so there are no obvious two stress peaks of the stress-strain curves. The UCS of samples controlled by shear crack is higher than that controlled by tensile crack, so the strength of specimen with $\beta = 0°$ is higher than that of other kinds of specimens.

After tensile cracks initiated and propagated, some shear crack branches initiated in the samples with flaw angle of 30°, 60°, and 90°. Tensile cracks are easier to initiate around the prefabricated crack than shear cracks. For the sample with $\beta = 30°$, a type III tensile crack initiated from tip of precrack firstly, and then multiple shear cracks initiated from upper boundary of the specimen, which are connected with the type III crack. For the sample with $\beta = 60°$, after type III and type I tensile cracks initiated from both tips of the prefabricated crack, one shear crack occurred at the upper part of the sample. For the sample with $\beta = 90°$, two type III tensile cracks initiated from the upper tip of prefabricated crack; after that, a type I tensile crack initiated and propagated downward toward the boundary of the sample from the middle of the prefabricated crack. Tensile cracks are the main kinds of crack in the samples with flaw angle of 30°, 60°, and 90°, and shear cracks are the minor kinds of crack. The σ-ε curves of samples with $\beta = 30°$, 45°, 60°, or 90° have two stress peaks because of phase propagation of cracks.

There is no obvious shear crack that appeared in the samples with $\beta = 45°$. Type III and I tensile crack initiated from both tips of the precrack, respectively. The number of new cracks in the sample with $\beta = 45°$ is less than that of other types of specimens, so the total energy required of sample with $\beta = 45°$ is the least. This is the important reason why the strength of the sample with $\beta = 45°$ is lower than other types of samples.

In accordance with Figure 12, under static loading, type I tensile crack at the lower part of the specimens with $\beta = 45°$, 60°, or 90° is closer to the middle of the precrack with the increase of the angle β. This phenomenon is consistent with the research results in [29]. In this paper, there are no obvious type IX far-field cracks and type IV mixed tensile-shear cracks and little type VII-VIII far-field shear cracks in the samples with different precracks under static loading.
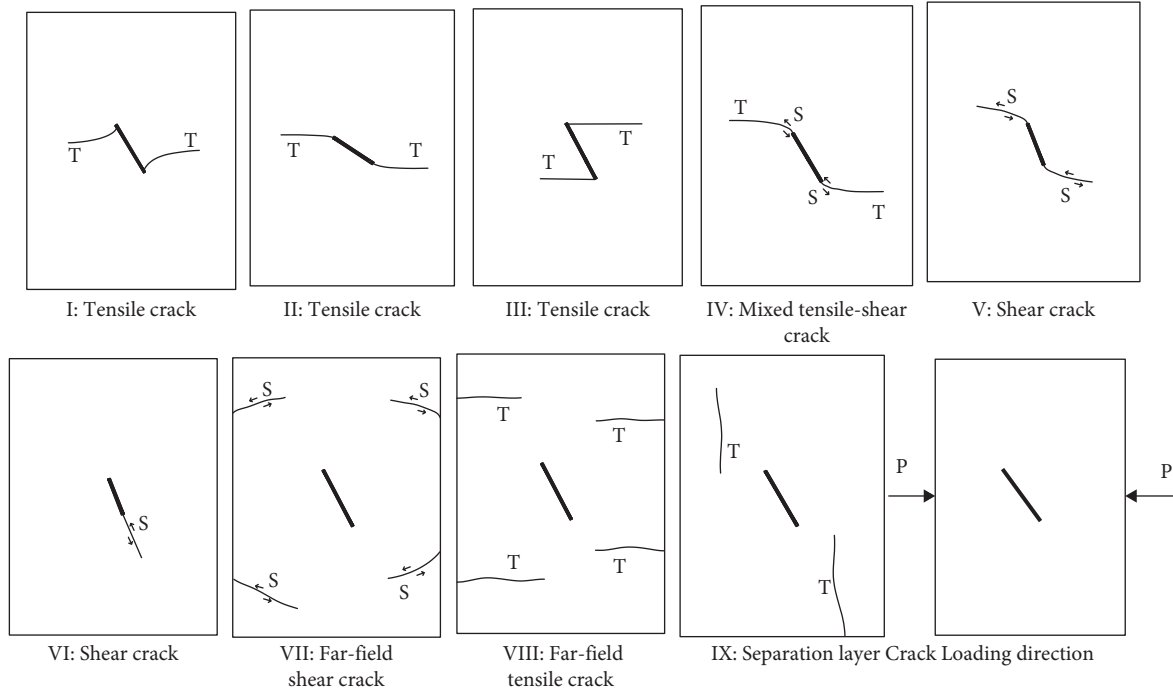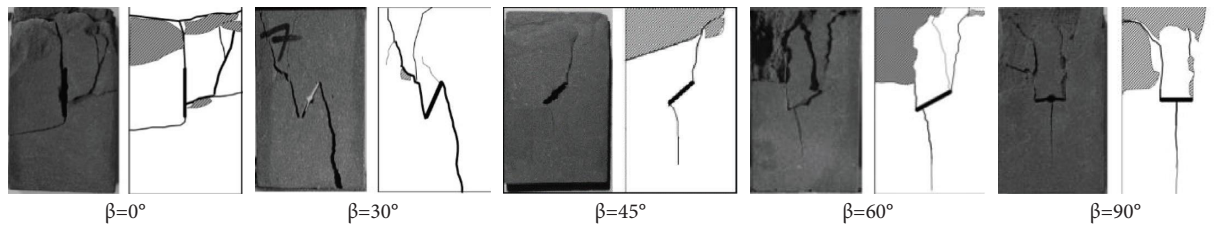
FIGURE 11: Types of crack propagation.

FIGURE 12: Failure modes of the single-flawed specimens.

4.2.2. Fracture Mode under Dynamic Impact Loading. The failure modes of the specimens are affected by strain rates and flaw inclination angles (Table 5). The crack types of different rock specimens under dynamic loading are listed in Table 6.

Under dynamic loading, with the increase of strain rate, much smaller sized fragments are produced, and the crack network of sample becomes more complex. When the peak of incident wave is 40.7 MPa, new crack was basically initiated around the prefabricated crack. Only one main crack propagated in each side of the prefabricated crack. The specimens with $\beta = 60°$ or $\beta = 90°$ were broken into two halves at failure, and the specimens with $\beta = 0°$, 30°, or 45° were broken into several major parts with small amount of pulverized rock debris. Only tensile crack propagation occurred in specimens with $\beta = 45°$ or 90° mainly. For specimens with $\beta = 0°$ or $\beta = 30°$, tensile and shear cracks are all the dominant kinds of crack. By contrast, pure shear fracture occurred only in specimens with $\beta = 60°$. When the peak of incident wave increases to 61.1 MPa, crack network of sample becomes more complex, generally showing "Y" shape crack bands. One or two main cracks propagated in each side of the precrack, and several far-field cracks

initiated. Type V shear crack became the main crack type except for specimens with flaw angle of 0°. More far-field shear cracks initiated in the specimens when the peak of incident wave was 61.1 MPa. Far-field tensile cracks appeared in specimens with flaw angle of 90° and penetrated the whole sample. When the peak of incident wave is 76.5 MPa, more far-field cracks appeared in the rock specimens. There are more shear cracks and fewer tensile cracks.

It was previously thought that shear cracks dominate the fracture mode of samples with single precrack [28], and the "X" shape crack band is generally the macroscopic failure mode when the rectangular plate specimen is used in the SHPB experiment [16]. The experimental results of this paper illustrate that for some samples of certain size, when the peak of incident wave is not very large, tensile cracks may dominate the fracture mode or several shear cracks form a "Y" shape failure pattern. Relevant studies [30, 31] have shown that when the strain rate ranges from $10^{-5}\,s^{-1}$ to $10^{-2}\,s^{-1}$ (low strain rate), with the increase of strain rate, the shear failure mode of single-flawed specimens changes to the tensile failure mode. By comparison, in the range of medium strain rate, with the increase of strain rate, the failure mode

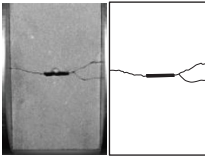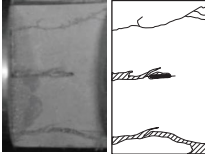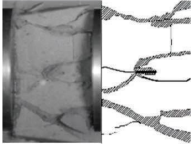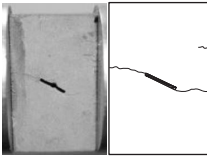TABLE 5: Final failure modes of samples under dynamic impact loading.
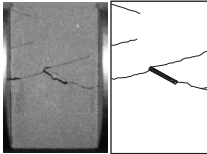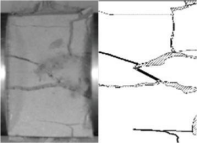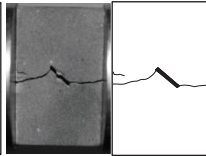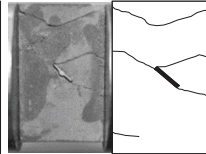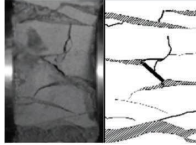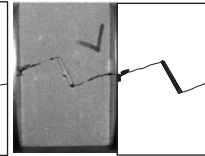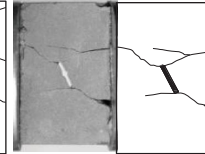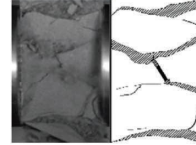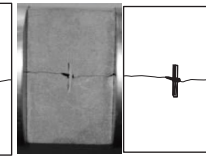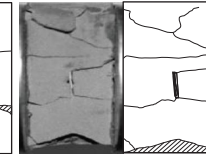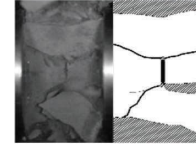
β	40.7 MPa	Peak of incident wave 61.1 MPa	76.5 MPa
0°			
30°			
45°			
60°			
90°			

TABLE 6: Crack types of different kinds of rock samples.

β (°)	0	30	45	60	90
Peak of incident wave 40.7 MPa	II, IV	III, V	III	V	I
Peak of incident wave 61.1 MPa	II, V, VII	V, VII	II, V, VII	V, VII	I, V, VII, VIII
Peak of incident wave 76.5 MPa	IV, V, II, VII, VIII, IX	III, V, VI, VII, VIII, IX	II, III, VII, VIII, IX	V, VII, IX	V, VII, VIII

of single-flawed specimens changes from tensile failure (except for $\beta = 60°$) to X-type shear failure, according to Table 5.

4.3. Crack Growth Process. Crack growth processes of specimens caused by dynamic loading are shown in Figure 13, when the peak of incident wave increases to 76.5 MPa. Various shear and tensile cracks constituted complex crack network of the samples. Tensile crack propagation is often restricted by shear crack. Shear cracks generally form an "X" shape failure pattern, and more far-field cracks appeared. The incident energy is relatively high, so more random far-field cracks generate in sample except for crack network around the prefabricated crack. Due to the nonuniformity of primary defects and new cracks in samples, the travel of stress waves inside the specimen was affected, resulting in the fracture degree of the part of the specimen near the incident bar being generally greater. Tensile stress along the axial direction, caused by the travel of stress wave in the sample, leads to the occurrence of separation layer crack (type IX tensile crack), which is almost absent when the peak of incident wave is 40.7 MPa or 61.1 MPa.

There are three stages in the crack growth process of samples with single precrack under impact load. First, cracks initially generate around the preexisting flaw tips except for a few samples. Second, the first shear crack continues to grow, while other tensile or shear cracks initiate and develop. Meanwhile, the precrack collapses and closes. Finally, far-field shear or tensile cracks propagate and connect with each other. In contrast, under quasi-static loading, collapsion of precrack is not obvious.

The type and initiation position of the first cracks for samples with different flaw are different under quasi-static or dynamic loading conditions. Under static loading, the first crack of all the kinds of rock samples in this paper generates around the precrack. Nevertheless, under impact load, the first crack may initiate away from the prefabricated crack. Shear cracks initially generate around the precrack tips except for the sample with $\beta = 0°$ which shows that far-field cracks initiate firstly when the peak of incident wave is 76.5 MPa. By contrast, when the peak of incident wave is 40.7 MPa or 61.1 MPa, cracks generate firstly at the preexisting crack tips in samples with $\beta = 0°$. Under dynamic loading, characteristics of the first cracks are listed as follows:

(1) In general, the first crack propagation is always accompanied by the collapse of the prefabricated crack. In contrast, under static loading, the collapsion of the precrack almost never occurred.

(2) When the peak of incident wave is 76.5 MPa or 61.1 MPa, in most cases, the propagation path of the first crack is not parallel to the dynamic impact direction. This phenomenon is contrary to that of the first crack propagation under quasi-static loading. When the peak of incident wave drops to 40.7 MPa, the propagation path of the first crack is roughly parallel to the impact direction except for the samples with $\beta = 60°$.

(3) When the peak of incident wave is 76.5 MPa, for the samples with $\beta = 90°$, the first cracks generate far away from the precrack, which are roughly parallel to the dynamic impact direction. The initiation of the first far-field cracks is also along with the broken of precrack itself.

5. Fragmentation Characteristics and Energy Evolution

5.1. Fragmentation Characteristics Affected by the Strain Rate and Preexisting Flaw Angle. The sample fragments were screened for quantifying the influences of preexisting flaw and loading rate on the fragment distribution of single-flawed samples, and the fractal theory is used to quantitatively analyze the degree of fragmentation. The aperture sizes of these sieves are 40 mm, 30 mm, 20 mm, 10 mm, 5 mm, and 1 mm, respectively. Fractal theory is used widely to characterize the distribution of rock fragment [32], which can be expressed as follows:

$$\lg Y = \lg \left[\frac{M(x)}{M_T} \right] = (3 - D_b) \lg \left(\frac{x}{x_m} \right), \qquad (3)$$

where D_b denotes fractal dimension, x and x_m denote granular size and maximum fragment dimension, respectively, $M(x)$ and M_T, respectively, denote the cumulative mass of broken particles smaller than x and the total mass of rock debris, and Y denotes lumpiness.

Photos of rock fragments after sieving under different peak of incident waves are shown in Table 7. Under impact load condition, loading rate obviously influences the debris characteristics of single-flawed samples. The experiments found that under a lower peak of incident wave, the single-flawed specimens break into two or several large fragments. However, when the peak of incident wave is relatively high, single-flawed specimens break into smaller fragments. With the increasing peak of incident wave, the rock sample is more fragmented. The high absorption energy promotes the growth of cracks, resulting in more fractured samples. At a given peak of incident wave, it can be observed that the preexisting flaw angle has significant influence on the debris characteristics in these tests.
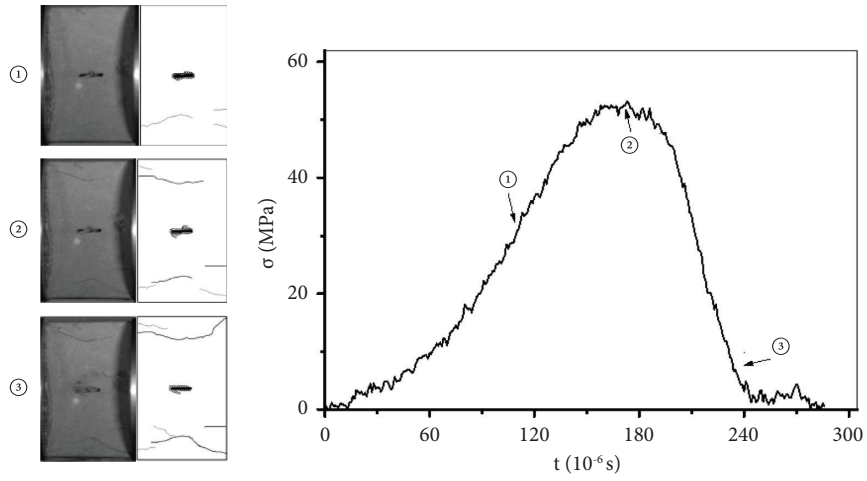
(a)
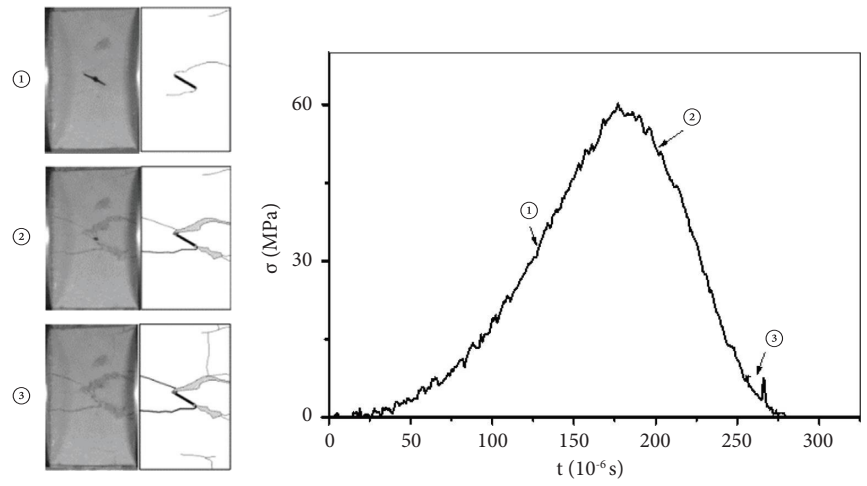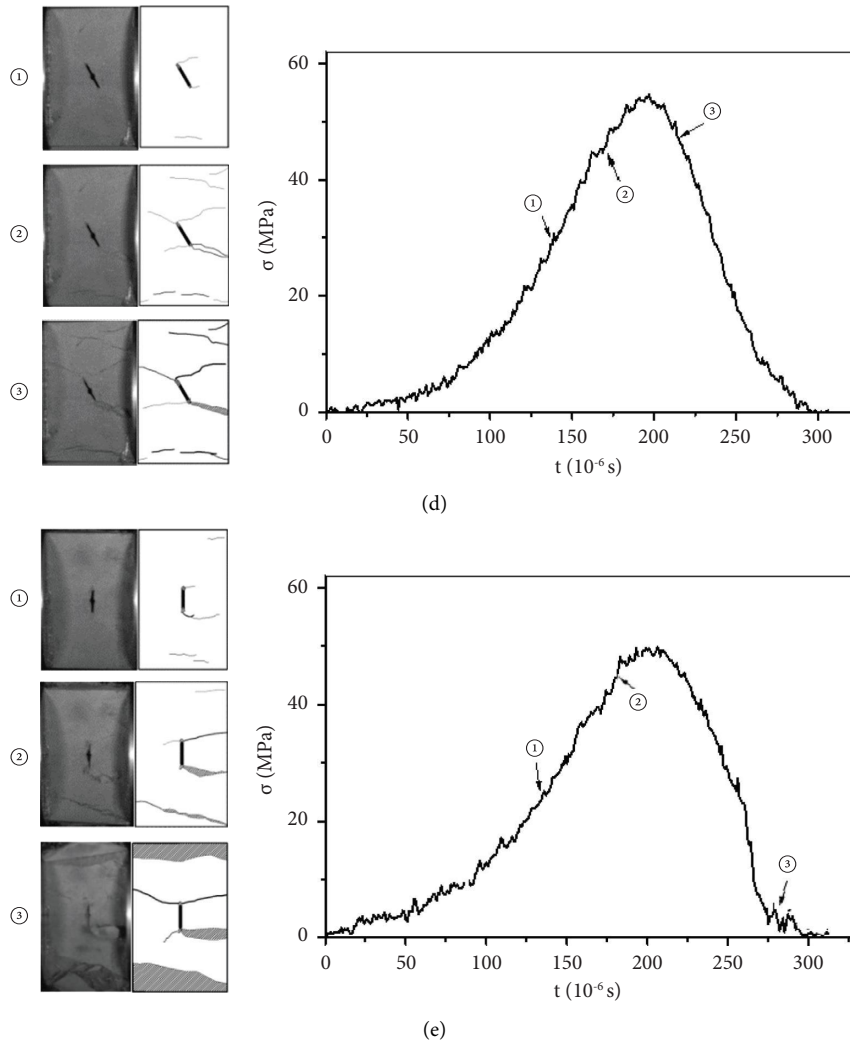

(b)
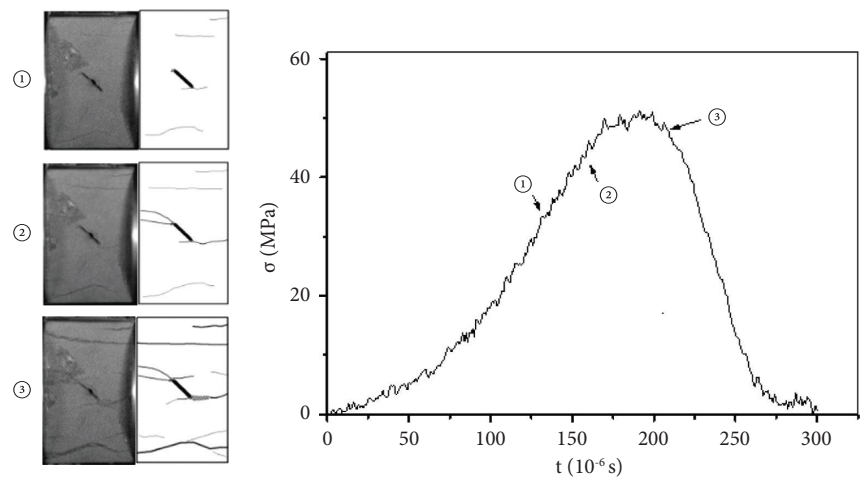
(c)

Figure 13: Continued.

(d)

(e)

Figure 13: Relationship between crack propagation process and stress. (a) $\beta = 0°$. (b) $\beta = 30°$. (c) $\beta = 45°$. (d) $\beta = 60°$. (e) $\beta = 90°$.

Table 7: The sieving of samples with different strain rates and cracks.

β (°)	Peak of incident wave		
	40.7 MPa	61.1 MPa	76.5 MPa
0			
30			

TABLE 7: Continued.
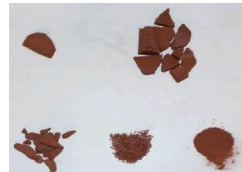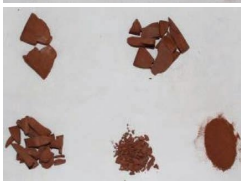
β (°)	Peak of incident wave		
	40.7 MPa	61.1 MPa	76.5 MPa
45			
60			
90			

TABLE 8: Fractal dimension of samples under different impact velocities.

Specimen number	D_b
D-0-4	1.28
D-0-5	1.40
D-0-6	1.28
D-0-7	2.07
D-0-8	1.89
D-0-9	1.89
D-0-10	2.54
D-0-11	2.50
D-0-12	2.56
D-30-4	1.29
D-30-5	1.33
D-30-6	1.25
D-30-7	1.78
D-30-8	1.85
D-30-9	1.87
D-30-10	2.20
D-30-11	2.14
D-30-12	2.22
D-45-4	1.25
D-45-5	1.29
D-45-6	1.26
D-45-7	1.63
D-45-8	1.57
D-45-9	1.62
D-45-10	2.14
D-45-11	2.17
D-45-12	2.15
D-60-4	1.31
D-60-5	1.22
D-60-6	1.40
D-60-7	2.05
D-60-8	2.06
D-60-9	2.16
D-60-10	2.42

TABLE 8: Continued.

Specimen number	D_b
D-60-11	2.46
D-60-12	2.35
D-90-4	1.25
D-90-5	1.33
D-90-6	1.33
D-90-7	2.05
D-90-8	2.04
D-90-9	2.01
D-90-10	2.22
D-90-11	2.14
D-90-12	2.25

The fractal dimensions of rock samples are determined using equation (3). In a coordinate system where $\lg[M(x)/M_T]$ is the x-coordinate and $\lg(x)$ is the y-coordinate, the slope of the line according to equation (3) is $3\text{-}D_b$, and the fractal dimension (D_b) of rock fragments can be obtained. Under different peaks of incident waves, fractal dimensions (D_b) of specimens with different precracks are shown in Table 8. Influences of precrack angle and dynamic strain rate on fractal dimension are shown in Figures 14 and 15, respectively.

As peak of incident wave increases, the fractal dimension of single-flawed specimens increases. When the peak of incident wave is 40.7 MPa, the fractal dimension of single-flawed specimens is between 1.22 and 1.40. When the peak of incident wave increases to 76.5 MPa, the fractal dimension is between 2.14 and 2.56, showing an evident strain rate dependence. Fractal dimension is larger, the distinct self-similarity is more, and fragment distribution is more homogeneous. Under a lower peak of incident wave, the energy supplied from the outside moves to preexisting and new flaw tips and produces some crack
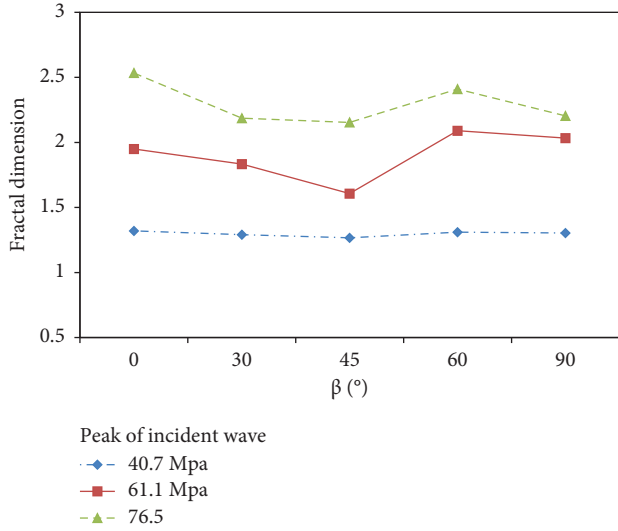
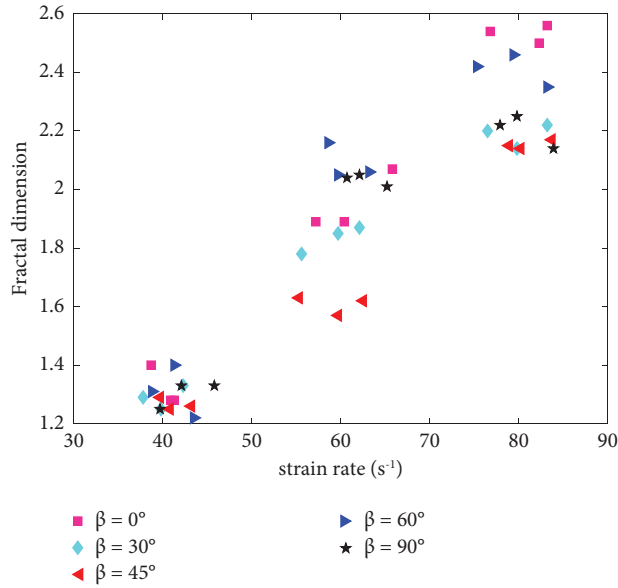FIGURE 14: Relationship between fractal dimension and crack dip angle.

FIGURE 15: Relationship between fractal dimension and strain rate.

TABLE 9: Energy indexes of samples.

Specimen number	W_i (J)	W_s (J)	η	e (J/cm^3)
D-0-4	30.00	11.96	0.40	0.59
D-0-5	28.73	10.97	0.38	0.55
D-0-6	28.84	11.08	0.38	0.61
D-0-7	58.55	25.77	0.44	1.44
D-0-8	63.09	26.92	0.43	1.24
D-0-9	60.40	26.20	0.43	1.32
D-0-10	94.50	45.92	0.49	1.55
D-0-11	92.00	45.96	0.50	1.79
D-0-12	98.56	50.70	0.51	1.76
D-30-4	24.89	9.52	0.38	0.51
D-30-5	31.42	12.27	0.39	0.55
D-30-6	26.13	9.64	0.37	0.50
D-30-7	63.09	26.10	0.41	1.19
D-30-8	65.34	28.41	0.43	1.36
D-30-9	56.58	24.58	0.43	1.20
D-30-10	105.00	48.43	0.46	2.30
D-30-11	95.44	45.16	0.47	2.06
D-30-12	97.68	47.78	0.49	2.08
D-45-4	31.56	12.42	0.39	0.43
D-45-5	28.26	11.13	0.39	0.49
D-45-6	32.78	13.00	0.40	0.39
D-45-7	63.18	26.99	0.43	1.09
D-45-8	57.12	25.16	0.44	1.13
D-45-9	57.24	25.63	0.45	1.19
D-45-10	100.80	49.78	0.49	2.09
D-45-11	97.82	46.65	0.48	2.05
D-45-12	104.39	49.94	0.48	1.76
D-60-4	30.16	12.20	0.40	0.75
D-60-5	30.29	12.20	0.40	0.60
D-60-6	27.24	10.72	0.39	0.61
D-60-7	62.80	27.80	0.44	1.21
D-60-8	60.50	27.94	0.46	1.36
D-60-9	57.50	25.75	0.45	1.35
D-60-10	101.40	53.16	0.52	2.29
D-60-11	104.58	53.80	0.51	2.27
D-60-12	99.00	48.48	0.49	2.18
D-90-4	28.88	11.65	0.40	0.56
D-90-5	31.89	13.19	0.41	0.72
D-90-6	30.48	12.43	0.41	0.79
D-90-7	62.64	29.00	0.46	1.14
D-90-8	58.25	27.62	0.47	1.34
D-90-9	62.40	27.92	0.45	1.25
D-90-10	105.70	52.34	0.50	2.20
D-90-11	99.90	52.20	0.52	2.27
D-90-12	103.04	55.06	0.53	2.21

tracks. The surface energy of these new appeared flaws consumes the energy transferring to flaw tips, so there are only a few new cracks. Under a higher peak of incident wave, the external energy is relatively high, resulting in producing abundant new cracks and fracture surface and inducing the samples to form mass rock debris. In this case, samples are characterized by smaller fragments. If fractal dimension is higher, the fragment distribution will be more uniform.

When the peak of incident wave is 40.7 MPa, the fractal dimensions of specimen with different flaw angles are similar. With the increase of the peak of incident wave, fractal dimension of specimen is obviously affected by the change of flaw angle. Under a given incident wave with a peak of 61.1 MPa or 76.5 MPa, the fractal dimensions of

specimen with $\beta = 45°$ are generally lower than those of the other specimens. It indicates that under impact load, the rock debris distribution of the specimens with $\beta = 45°$ is most inhomogeneous.

5.2. Energy Evolution under Dynamic Impact Loading. Rock failure caused by crack connection and propagation is essentially an energy dissipation process. Energies can be represented by incident wave $\varepsilon_I(t)$, reflected wave $\varepsilon_R(t)$, and transmitted wave $\varepsilon_T(t)$ collected during the SHPB tests. The relevant energy (incident energy (W_i), transmitted energy (W_t), and reflected energy (W_r)) can be calculated as follows:
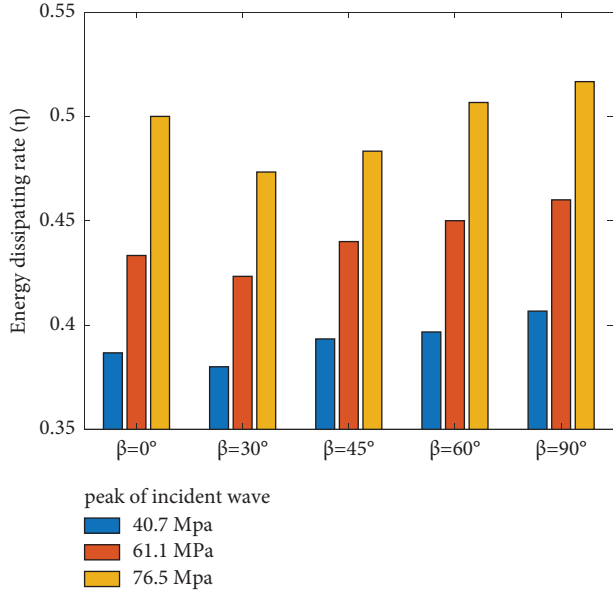
FIGURE 16: Energy dissipating rate under different strength impact loads.

FIGURE 17: Energy dissipation density under different strength impact loads.

$$W_i(t) = E_e C_e A_e \int_0^t \varepsilon_I^2(t)dt, \qquad (4)$$

$$W_t(t) = E_e C_e A_e \int_0^t \varepsilon_T^2(t)dt, \qquad (5)$$

$$W_r(t) = E_e C_e A_e \int_0^t \varepsilon_R^2(t)dt. \qquad (6)$$

The dissipated energy (W_s) of specimens includes three aspects: energy to fracture, the kinetic energy of splinters, and the dissipated energy depending on acoustic emission and heat. If the energy loss between the specimen and the bar is ignored, the energy W_s can be calculated as follows:

$$W_s(t) = W_i(t) - W_r(t) - W_t(t). \qquad (7)$$

During the SHPB tests, energy absorption is an important feature, which is closely connected with the surface area and number of new defects in samples. The density of energy dissipation (e) and the energy dissipating rate (η) of specimens can be calculated as follows:

$$e = \frac{W_s}{V}, \qquad (8)$$

$$\eta = \frac{W_s}{W_i}, \qquad (9)$$

where V denotes the volume of rock sample. The relevant energy indexes obtained by equations (4)–(9) are listed in Table 9.

As the peak of incident wave increases, the W_i value and W_s value increase significantly. The energy dissipating rate (average of three samples) under various strength impact loads is plotted in Figure 16. The energy dissipating rate is closely related to peak of incident wave. The single-flawed
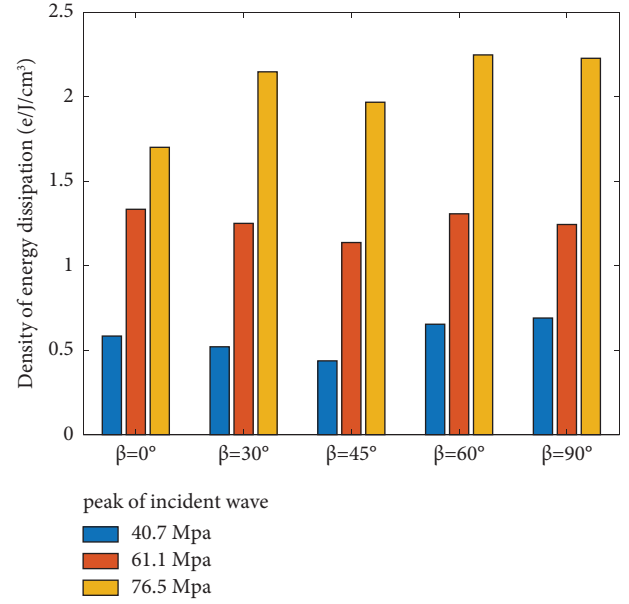
specimen with $\beta = 90°$ is the kind of specimen having most dissipating rate, which varies from 0.40 to 0.53. Obviously, the energy dissipating rate of single-flawed specimens can be improved in a certain range of strain rate under external dynamic impact loading. Figure 17 presents the effect of peak of incident wave on the e value (average of three samples) of single-flawed specimens. As the peak of incident wave increases, the e value increases obviously. The e value of the single-flawed sample with $\beta = 45°$ is the lowest among all kinds of samples when the peak of incident wave is 40.7 MPa and 61.1 MPa. With the increase of incident wave peak, the difference of energy dissipation density of samples with various β values is more obvious. When the peak of incident wave is 76.5 MPa, the single-flawed sample with $\beta = 0°$ has the lowest energy dissipation density. It indicates that the e value of the single-precrack specimens features a rising trend with the increase of incident wave peak, and the influence of precrack angle on energy dissipation is significant for a given peak of incident wave.

There are relationships between the energy dissipation and the failure modes. The number and development of cracks is related to the density of energy dissipation. The density of energy dissipation is less when the sample has fewer cracks and is broken into several parts. On the contrary, when the sample has more cracks and is completely crushed, the density of energy dissipation will increase significantly.

6. Discussion

Microcrack development from tips of precrack and coalescence with branching cracks in rock specimens lead to the ultimate destruction of samples. Macroproperties of specimens could be shown by dynamic strength, energy dissipation, and fragment distribution. The interrelations of these parameters are shown in Figure 18.
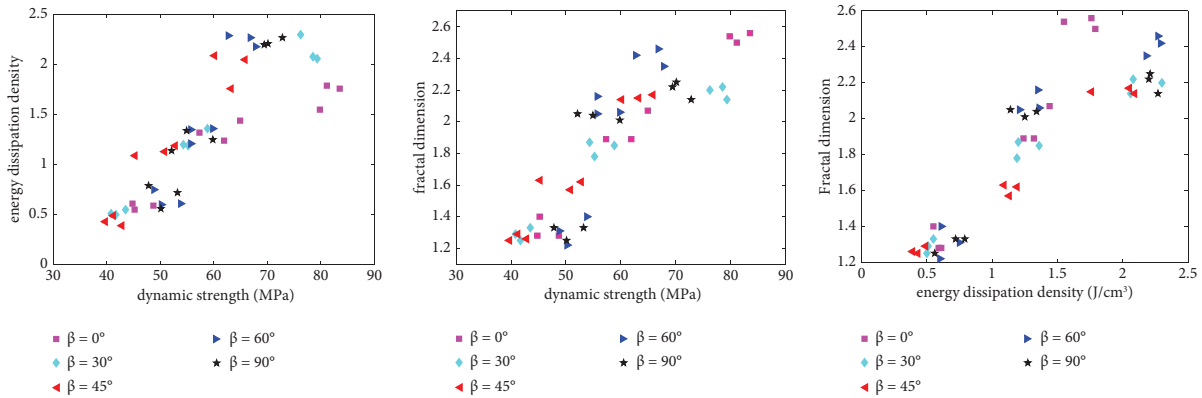
FIGURE 18: The interrelation of strength, energy dissipation, and fragment distribution.

The strength, energy dissipation, and fractal dimension of the rock samples are positively correlated with each other under different strength impact loading. For all kinds of rock samples with a certain precrack in this study, with the increase of dynamic strength, the average energy dissipation density of samples and fractal dimension increase. For a given peak of incident wave, as the energy dissipation density increases, the fractal dimension also increases. When the peak of incident wave is low (40.7 MPa), the effect of precrack angle on the relationships between these three parameters of rock specimens is not significant. As the peak of incident wave increases, the angle of precrack has more important impact on the interrelation of these three parameters.

High strain rate (the peak of incident wave is high) has enhancement effect on the three parameters of rock specimens with precrack. According to the rock fracture theory [33], the relationship between the fragment size, size of the intergranular cracks, and length of crack propagation can be understood. Under stronger impact loading, with the increase of the peak of incident wave, more energy is absorbed for crack initiation, which also causes more tiny cracks to expand, resulting in generation of more small rock debris. Under this condition, more microstructures of the specimen take part in resistance to break, causing increase of the dynamic macrostrength of the specimen. The precrack guides the initiation of the main crack in the rock specimen, so it influences the relationship between these three parameters, together with the strain rate.

7. Conclusions

Under static loading, with the increase of precrack angle, the static strength and static modulus of elasticity of single-flawed rock specimen decrease first and then increase. The ultimate crack network of the samples contains several types of cracks, such as types I, II, III, V, and VI. In general, after new tensile cracks initiated around the prefabricated crack, some shear crack branches initiated in the samples except for the specimen with $\beta = 0°$.

Under impact dynamic loading, when the strain rate increases, the dynamic strength and modulus increase significantly, whose change trend also depends on the angle of

precrack in specimens. With the increase of strain rate, crack network of sample becomes more complex. Shear cracks usually dominate the fracture mode of single-flawed specimens and form an "X" shape failure pattern, but when the peak of incident wave is not very large, tensile cracks may dominate the fracture mode or several shear cracks form a "Y" shape failure pattern.

Under impact dynamic loading, with the increasing peak of incident wave, the fractal dimension of single-flawed specimens increases. When the strain rate increases, the fractal dimension of specimen is obviously affected by the change of flaw angle. The energy dissipation density and energy dissipating rate of single-flawed samples show an increasing trend with the increasing peak of incident wave. The influence of inclination angle of precrack on the energy dissipation is significant for a given peak of incident wave.

The strength, energy dissipation, and fractal dimension of the rock samples are positively correlated with each other under different strength impact loading. The larger the peak value of incident wave, the more significant the precrack angle on the interrelation of these three parameters.

Data Availability

The data used to support the findings of this study are included within the article.

Conflicts of Interest

The authors declare that they have no conflicts of interest.

Acknowledgments

References

[1] Z. Z. Liang, H. Xing, S. Y. Wang, D. J. Williams, and C. A. Tang, "A threedimensional numerical investigation of the fracture of rock specimens containing a pre-existing

surface flaw," *Computers and Geotechnics*, vol. 45, no. 45, pp. 19–33, 2012.

[2] Q. H. Wu, C. L. Xie, Y. S. Xie et al., "Extending application of asymmetric semi-circular bend specimen to investigate mixed mode I/II fracture behavior of granite," *Journal of Central South University*, vol. 29, no. 4, pp. 1289–1304, 2022.

[3] S. Q. Yang, Y. H. Huang, W. L. Tian, and J. B. Zhu, "Erratum to: an experimental investigation on strength, deformation and crack evolution behavior of sandstone containing two oval flaws under uniaxial compression," *Engineering Geology*, vol. 217, pp. 35–48, 2017.

[4] A. Bobet and H. H. Einstein, "Fracture coalescence in rock-type materials under uniaxial and biaxial compression," *International Journal of Rock Mechanics and Mining Sciences*, vol. 35, no. 7, pp. 863–888, 1998.

[5] H. Jiefan, C. Ganglin, Z. Yonghong, and W. Ren, "An experimental study of the strain field development prior to failure of a marble plate under compression," *Tectonophysics*, vol. 175, no. 1-3, pp. 269–284, 1990.

[6] H. Haeri, K. Shahriar, M. F. Marji, and P. Moarefvand, "On the strength and crack propagation process of the pre-cracked rock-like specimens under uniaxial compression," *Strength Mater*, vol. 46, no. 1, pp. 140–152, 2014.

[7] X. P. Zhou, H. Cheng, and Y. F. Feng, "An experimental study of crack coalescence behaviour in rock-like materials containing multiple flaws under uniaxial compression," *Rock Mechanics and Rock Engineering*, vol. 47, no. 6, pp. 1961–1986, 2014.

[8] Y. Sheng-Qi and J. Hong-Wen, "Strength failure and crack coalescence behavior of brittle sandstone samples containing a single fissure under uniaxial compression," *International Journal of Fracture*, vol. 2, pp. 227–250, 2011.

[9] C. Zhao, F. Liu, J. Tian, H. Matsuda, and C. Morita, "Study on single crack propagation and damage evolution mechanism of rock-like materials under uniaxial compression," *Chinese Journal of Rock Mechanics and Engineering*, vol. 35, no. Supp.2, pp. 3 626–633 632, 2016.

[10] X. Li, T. S. Lok, and J. Zhao, "Dynamic characteristics of granite subjected to intermediate loading rate," *Rock Mechanics and Rock Engineering*, vol. 38, no. 1, pp. 21–39, 2005.

[11] Q. B. Zhang and J. Zhao, "A review of dynamic experimental techniques and mechanical behaviour of rock materials," *Rock Mechanics and Rock Engineering*, vol. 47, no. 4, pp. 1411–1478, 2014.

[12] D. Y. Li, Z. Y. Han, X. L. Sun, T. Zhou, and X. B. Li, "Dynamic mechanical properties and fracturing behavior of marble specimens containing single and double flaws in SHPB tests," *Rock Mechanics and Rock Engineering*, vol. 52, no. 6, pp. 1623–1643, 2019.

[13] B. J. Xie, D. H. Ai, and Y. Yu, "Crack detection and evolution law for rock mass under SHPB impact tests," *Shock and Vibration*, vol. 2019, Article ID 3956749, 12 pages, 2019.

[14] D. H. Ai, Y. C. Zhao, Q. F. Wang, and C. W. Li, "Experimental and numerical investigation of crack propagation and dynamic properties of rock in SHPB indirect tension test," *International Journal of Impact Engineering*, vol. 126, pp. 135–146, 2019.

[15] D. Li, Q. Zhu, Z. Zhou, X. Li, and P. G. Ranjith, "Fracture analysis of marble specimens with a hole under uniaxial compression by digital image correlation," *Engineering Fracture Mechanics*, vol. 183, pp. 109–124, 2017.

[16] C. Zou, L. N. Y. Wong, J. J. Loo, and B. S. Gan, "Different mechanical and cracking behaviors of single-flawed brittle gypsum specimens under dynamic and quasi-static loadings," *Engineering Geology*, vol. 201, pp. 71–84, 2016.

[17] P. Dong, B. Wu, K. Xia, and Q. Wang, "Fracture modes of single-flawed rock-like material plates subjected to dynamic compression," *International Journal of Geomechanics*, vol. 20, no. 9, pp. 1532–3641, 2020.

[18] Z. Han, D. Li, T. Zhou, J. Chen, and S. Xie, "Dynamic progressive fracture behavior of axially confined sandstone specimens containing a single flaw," *Theoretical and Applied Fracture Mechanics*, vol. 122, Article ID 103597, 2022.

[19] W. You, F. Dai, and Y. Liu, "Experimental and numerical investigation on the mechanical responses and cracking mechanism of 3D confined single-flawed rocks under dynamic loading," *Journal of Rock Mechanics and Geotechnical Engineering*, vol. 14, no. 2, pp. 477–493, 2022.

[20] Z. L. Yan, F. Dai, Y. Liu, A. Li, and H. Du, "Numerical assessment of the rate-dependent cracking behaviours of single-flawed rocks in split Hopkinson pressure bar tests," *Engineering Fracture Mechanics*, vol. 247, Article ID 107656, 2021.

[21] Q. H. Wu, L. Weng, Y. L. Zhao, and F. Feng, "Influence of infilling stiffness on mechanical and fracturing responses of hollow cylindrical sandstone under uniaxial compression tests," *Journal of Central South University*, vol. 28, no. 8, pp. 2485–2498, 2021.

[22] Y. Zhou, K. Xia, X. Li et al., "Suggested methods for determining the dynamic strength parameters and mode-I fracture toughness of rock materials," *International Journal of Rock Mechanics and Mining Sciences*, vol. 49, pp. 105–112, 2012.

[23] J. Qiu, D. Li, and X. Li, "Dynamic failure of a phyllite with a low degree of metamorphism under impact Brazilian test," *International Journal of Rock Mechanics and Mining Sciences*, vol. 94, pp. 10–17, 2017.

[24] Z. Zhou, X. Li, Z. Ye, and K. Liu, "Obtaining constitutive relationship for rate-dependent rock in SHPB tests," *Rock Mechanics and Rock Engineering*, vol. 43, no. 6, pp. 697–706, 2010.

[25] J. M. Lifshitz and H. Leber, "Data processing in the split Hopkinson pressure bar tests," *International Journal of Impact Engineering*, vol. 15, no. 6, pp. 723–733, 1994.

[26] Y. Zhou, S. Qian, and N. Li, "Dynamic increasing factor model for strength and modulus of rock materials at different strain rates," *Chinese Journal of Rock Mechanics and Engineering*, vol. 39, no. Suppl. 2, pp. 3 245–253 259, 2020.

[27] C. H. Park and A. Bobet, "Crack initiation, propagation and coalescence from frictional flaws in uniaxial compression," *Engineering Fracture Mechanics*, vol. 77, no. 14, pp. 2727–2748, 2010.

[28] X. B. Li, T. Zhou, and D. Y. Li, "Dynamic strength and fracturing behavior of single-flawed prismatic marble specimens under impact loading with a split-Hopkinson pressure bar," *Rock Mechanics and Rock Engineering*, vol. 50, no. 1, pp. 29–44, 2017.

[29] L. N. Y. Wong and H. H. Einstein, "Process zone development associated with cracking processes in carrara marble," *Analysis of discontinuous deformation: new developments and applications*, pp. 581–588, 2010.

[30] Q. F. Guo, X. Wu, M. F. Cai, X. Xi, and S. J. Miao, "Experiment on the strength characteristics and failure modes of granite with pre-existing cracks," *Chinese Journal of Engineering*, vol. 41, no. 1, pp. 43–52, 2019.

[31] Y. Zhao, L. Zhang, W. Wang, C. Pu, W. Wan, and J. Tang, "Cracking and stress–strain behavior of rock-like material containing two flaws under uniaxial compression," *Rock*

Mechanics and Rock Engineering, vol. 49, no. 7, pp. 2665–2687, 2016.

[32] T. Zhang, J. Chen, and X. Wang, "Study on the influence of different loading rates on the deformation characteristics of porous specimens," *Chinese Journal of Mining and Safety Engineering*, vol. 38, no. 04, pp. 847–856, 2021.

[33] L. Yu, Q. Yao, Q. Xu, W. Wang, Z. Niu, and W. Liu, "Experimental and numerical simulation study on crack propagation of fractured fine sandstone under the influence of loading rate," *Journal of Coal Society*, vol. 46, no. 11, pp. 3488–3501, 2021.

[34] M. Sharafisafa, Z. Aliabadian, and L. Shen, "Crack initiation and failure development in bimrocks using digital image correlation under dynamic load," *Theoretical and Applied Fracture Mechanics*, vol. 109, Article ID 102688, 2020.

[35] E. Eberhardt, B. Stimpson, and D. Stead, "Effects of grain size on the initiation and propagation thresholds of stress-induced brittle fractures," *Rock Mechanics and Rock Engineering*, vol. 32, no. 2, pp. 81–99, 1999.